Supporting Information

One-Step Microwave Synthesis of Boron-Doped BiOBr/rGO Nanohybrids with Enhanced Visible-Light Photocatalytic and Antibacterial Performance

Shanavas Yoosuf,[a] Muhammed Muhammed Safeer Naduvil Kovilakath,[b] Neena S. John,[b] and Shalina Begum Tharayil*[a]

[a]Postgraduate and Research Department of chemistry, Farook College (Autonomous), Affiliated to University of Calicut, 673632, Kerala, India

[b]Centre for Nano and Soft Matter Sciences (CeNS), Shivanapura, Bengaluru 562162, India.

E-mail: shalinat@gmail.com

Corresponding Author

Shalina Begum Tharayil - *Postgraduate and Research Department of chemistry, Farook College (Autonomous), Calicut 673632, Kerala, India. (Affiliated to University of Calicut)*

E-mail: shalinat@gmail.com

Table of Contents	
Table S1	Inoculums details.
Fig. S1	Elemental composition analysis of B-BiOBr/rGO composite material, as revealed by Energy-Dispersive Spectroscopy (EDS).
Fig. S2	Elemental composition analysis of BiOBr, as revealed by Energy-Dispersive Spectroscopy (EDS).
Fig. S3	Elemental composition analysis of BiOBr/rGO composite, as revealed by Energy-Dispersive Spectroscopy (EDS).
Fig. S4	Elemental composition analysis of B-BiOBr composite, as revealed by Energy-Dispersive Spectroscopy (EDS).
Fig. S5	Spatial distribution of elements within the B-BiOBr/rGO composite, as visualized through elemental mapping analysis.
Fig. S6	Spatial distribution of elements within the BiOBr, as visualized through elemental mapping analysis.
Fig. S7	Spatial distribution of elements within the BiOBr/rGO composite, as visualized through elemental mapping analysis.
Fig. S8	Spatial distribution of elements within the B-BiOBr composite, as visualized through elemental mapping analysis.
Fig. S9	(a) N_2 adsorption-desorption isotherms and (b) pore size distribution profiles of B-BiOBr/rGO, B-BiOBr, BiOBr/rGO, and BiOBr, illustrating their surface properties and pore structures.
Table S2	Summary of BET analysis results for modified photocatalysts, including specific surface area, pore size distribution, and total pore volume.
Fig. S10	Effect of pH on the photocatalytic degradation of (a) MB and (b) RhB using B-BiOBr/rGO as photocatalyst (c) The point of zero charge (pH_{PZC}) of B-BiOBr/rGO determined by the pH drift method.

Fig. S11	Impact of catalyst loading on the photocatalytic degradation of (a) MB and (b) RhB using B-BiOBr/rGO photocatalyst.
Fig. S12	Effect of initial dye concentration on the photocatalytic degradation of (a) MB and (b) RhB using B-BiOBr/rGO as the photocatalyst.
Fig. S13	Degradation efficiency and mineralization of (a) MB and (b) RhB by B-BiOBr/rGO under optimized conditions.
Fig. S14	XRD spectrum of B-BiOBr/rGO after photocatalytic activity studies.
Fig. S15	Effect of scavengers on the photocatalytic degradation of (a) MB and (b) RhB using B-BiOBr/rGO as the catalyst.
Fig. S16	LC–MS spectrum of methylene blue before light irradiation, showing the characteristic molecular ion peak of the parent dye.
Fig. S17	LC–MS spectrum of methylene blue after photocatalysis, illustrating the degradation of the parent dye into characteristic fragment ions.
Fig. S18	LC–MS spectrum of rhodamine B before light irradiation, showing the characteristic molecular ion peak of the parent dye.
Fig. S19	LC–MS spectrum of rhodamine B after photocatalysis, illustrating the degradation of the parent dye into characteristic fragment ions.
Fig. S20	Impact of varying concentrations of (a) BiOBr, (b) BiOBr/rGO, (c) B-BiOBr, and (d) B-BiOBr/rGO on the growth of Bacillus subtilis, a Gram-positive bacterium, at two different doses: 500 µg (T1) and 1000 µg (T2) per disc.
Fig. S21	Impact of varying concentrations of (a) BiOBr, (b) BiOBr/rGO, (c) B-BiOBr, and (d) B-BiOBr/rGO on the growth of Staphylococcus aureus, a Gram-positive bacterium, at two different doses: 500 µg (T1) and 1000 µg (T2) per disc.
Fig. S22	Impact of varying concentrations of (a) BiOBr, (b) BiOBr/rGO, (c) B-BiOBr, and (d) B-BiOBr/rGO on the growth of Pseudomonas Aerugnosa, a Gram-negative bacterium, at two different doses: 500 µg (T1) and 1000 µg (T2) per disc.

Fig. S23	Impact of varying concentrations of (a) BiOBr, (b) BiOBr/rGO, (c) B-BiOBr, and (d) B-BiOBr/rGO on the growth of Escherichia coli, a Gram-negative bacterium, at two different doses: 500 μg (T1) and 1000 μg (T2) per disc.
Fig. S24	Impact of varying concentrations of (a) BiOBr, (b) BiOBr/rGO, (c) B-BiOBr, and (d) B-BiOBr/rGO on the growth of Vibrio cholerae, a Gram-negative bacterium, at two different doses: 500 μg (T1) and 1000 μg (T2) per disc.
Table S3	Inhibition Zone Measurements for BiOBr, BiOBr/rGO, B-BiOBr, and B-BiOBr/rGO Against Different Bacterial Strains
Table S4	ICP–MS analysis of B–BiOBr/rGO after antibacterial studies, showing Bi ion concentration to evaluate material stability.
Table S5	ICP–MS analysis of B–BiOBr/rGO after photocatalytic degradation of methylene blue, demonstrating Bi ion release and structural stability of the composite.
Table S6	ICP–MS analysis of B–BiOBr/rGO after photocatalytic degradation of rhodamine B, demonstrating Bi ion release and structural stability of the composite.

Name of Microorganism	MTCC No.	Incubation conditions
Escherichia coli	443	37 °C for 24 hours
Vibrio cholerae	3906	
Staphylococcus aureus	87	
Pseudomonas aeruginosa	741	
Bacillus subtilis	2413	

Table S1 Inoculums details

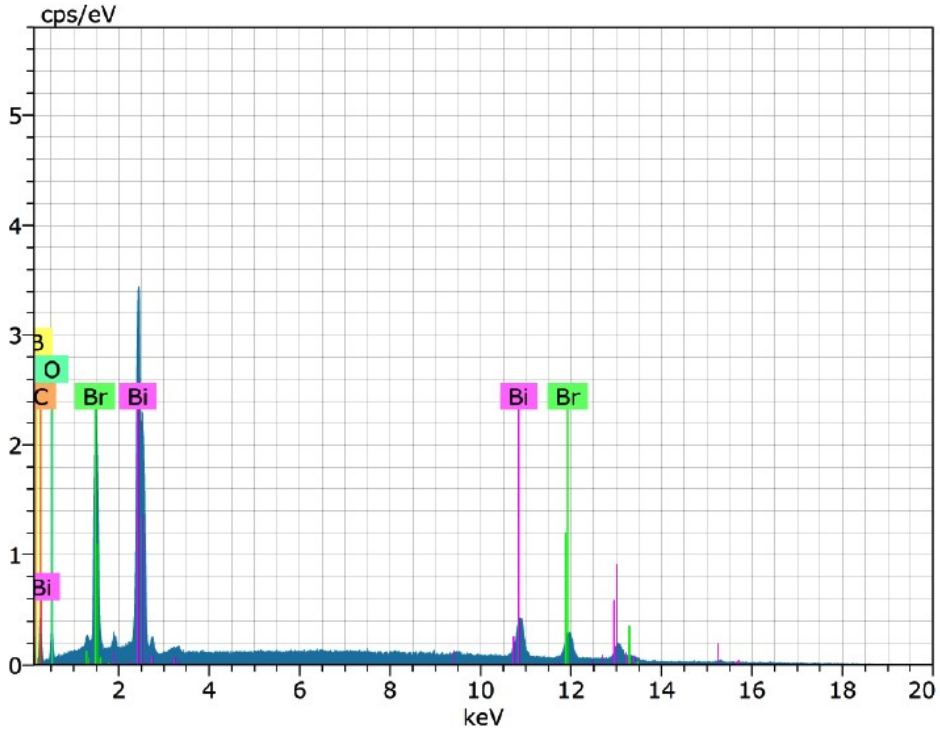

Fig. S1 Elemental composition analysis of B-BiOBr/rGO composite material, as revealed by Energy-Dispersive Spectroscopy (EDS).

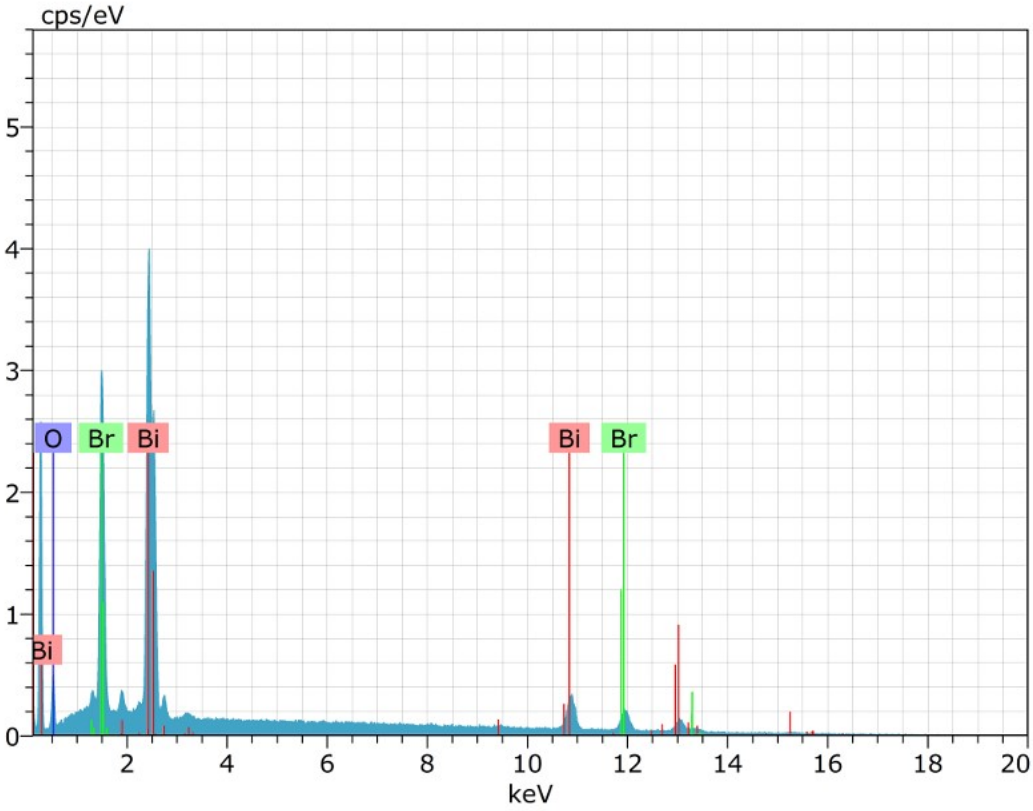

Fig. S2 Elemental composition analysis of BiOBr, as revealed by Energy-Dispersive Spectroscopy (EDS).

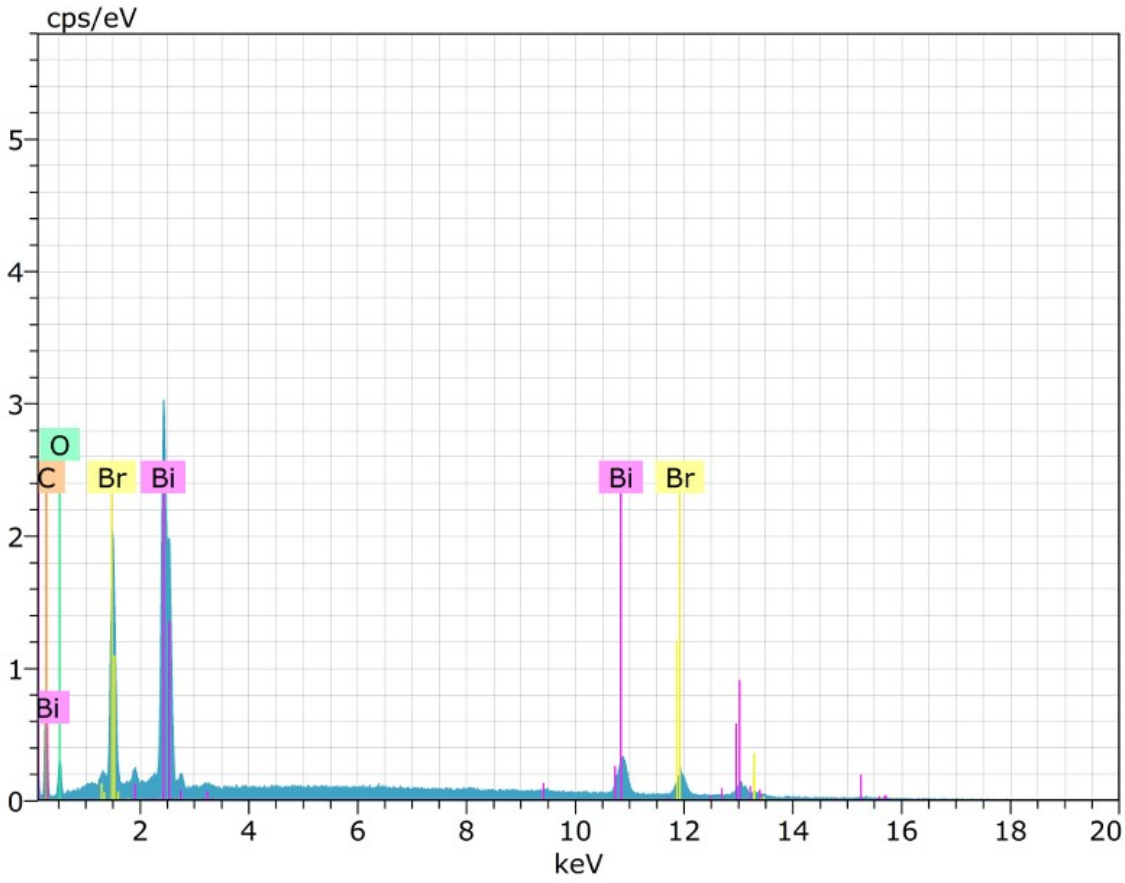

Fig. S3 Elemental composition analysis of BiOBr/rGO composite, as revealed by Energy-Dispersive Spectroscopy (EDS).

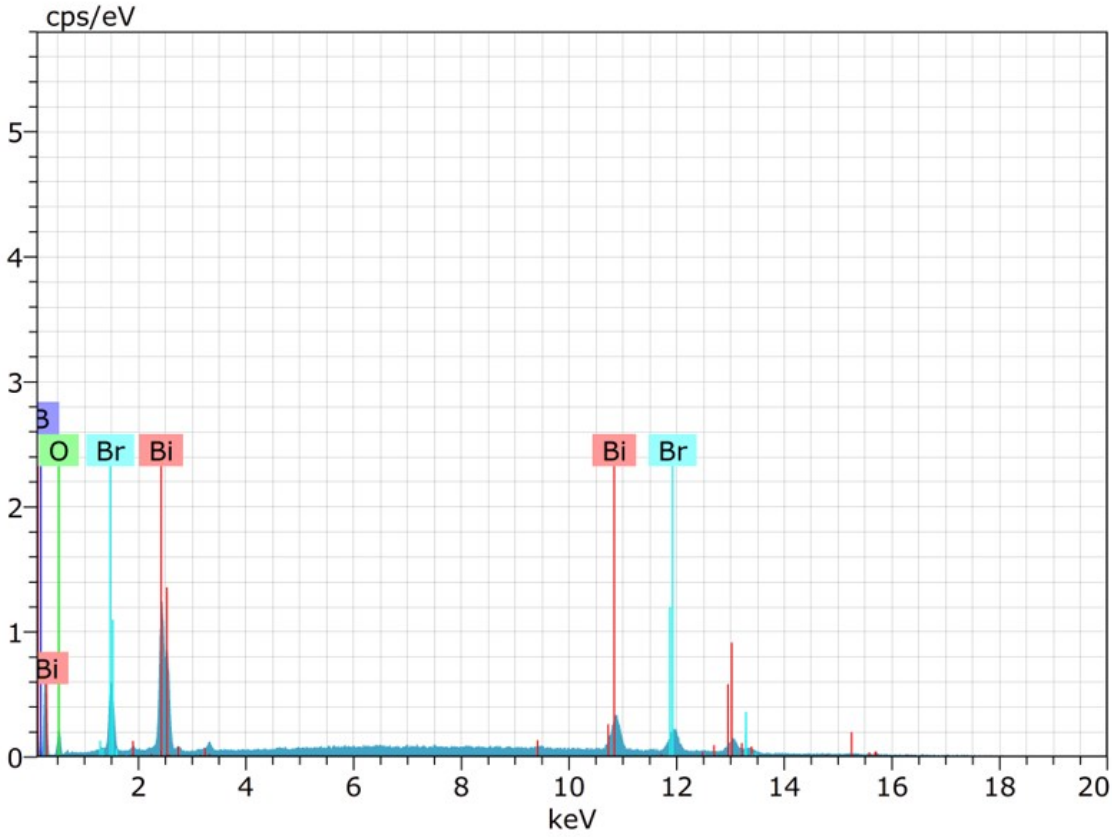

Fig. S4 Elemental composition analysis of B-BiOBr, as revealed by Energy-Dispersive Spectroscopy (EDS).

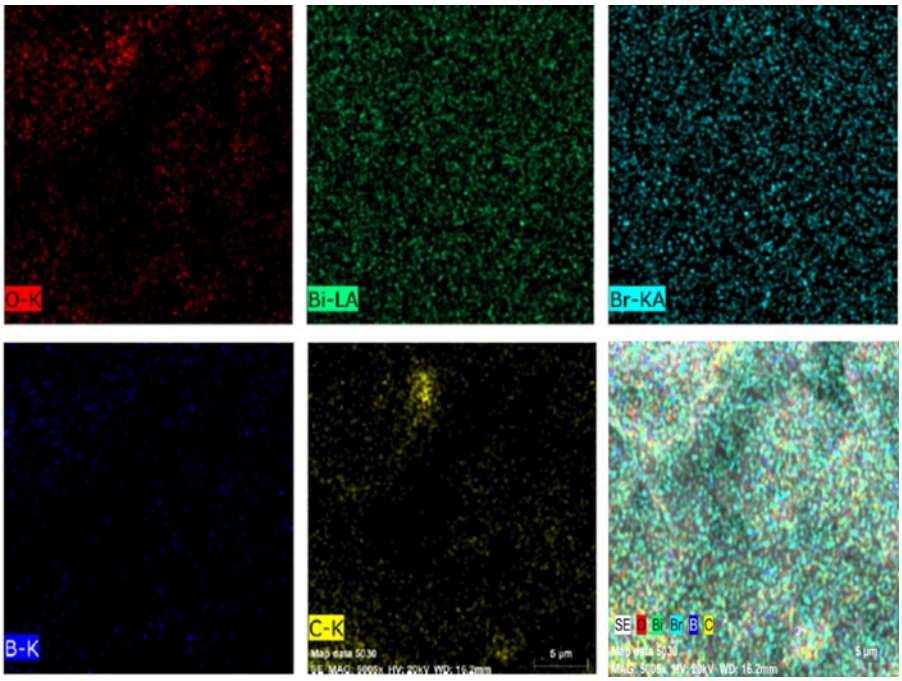

Fig. S5 Spatial distribution of elements within the B-BiOBr/rGO composite, as visualized through elemental mapping analysis.

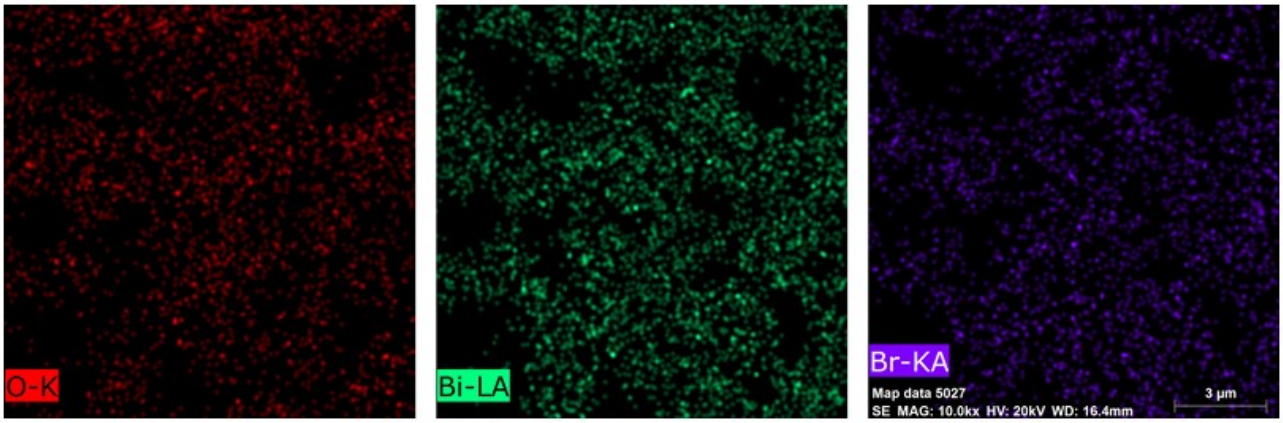

Fig. S6 Spatial distribution of elements within the BiOBr, as visualized through elemental mapping analysis.

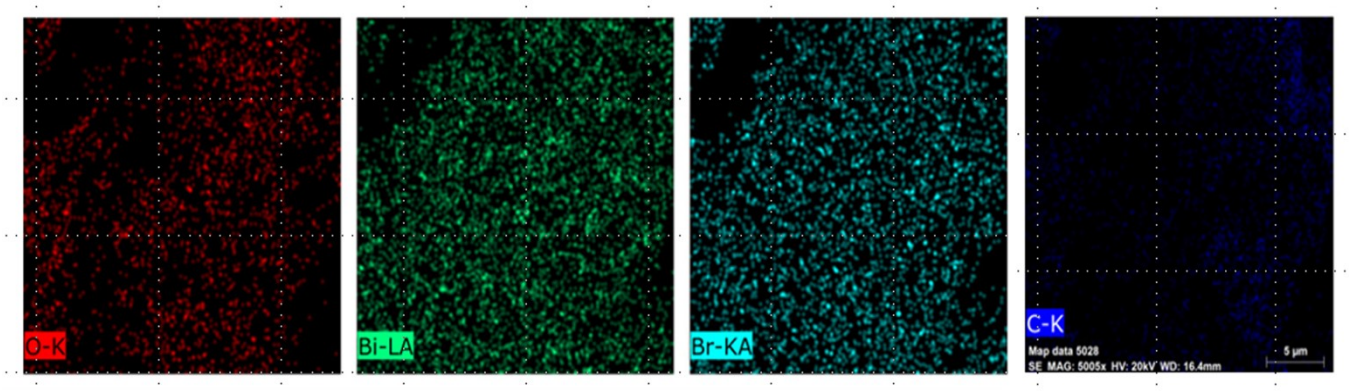

Fig. S7 Spatial distribution of elements within the BiOBr/rGO composite, as visualized through elemental mapping analysis.

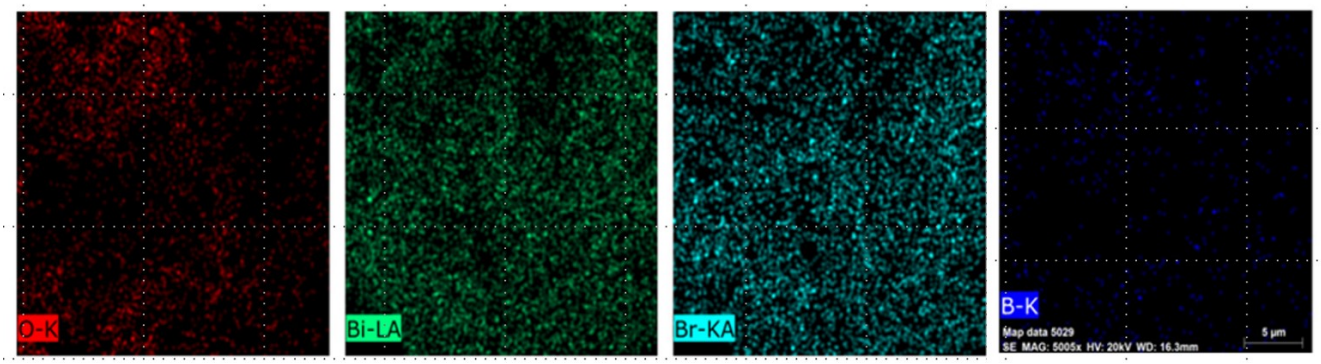

Fig. S8 Spatial distribution of elements within the B-BiOBr composite, as visualized through elemental mapping analysis.

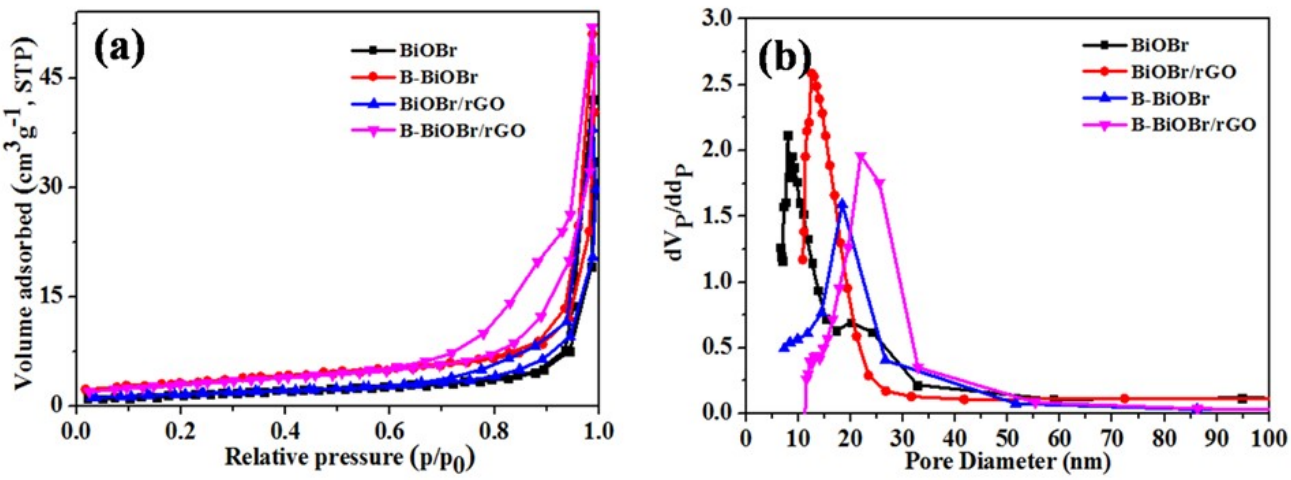

Fig. S9 (a) N_2 adsorption-desorption isotherms and (b) pore size distribution profiles of B-BiOBr/rGO, B-BiOBr, BiOBr/rGO, and BiOBr, illustrating their surface properties and pore structures.

Catalysts	BET Surface Area (m^2/g)	BJH Pore Size Distribution (nm)	Total Pore Volume (cm^3/g)
BiOBr	7.64	12.29	0.125
BiOBr/rGO	11.55	13.01	0.196
B-BiOBr	13.42	18.42	0.247
B-BiOBr/rGO	19.78	21.95	0.321

Table S2 Summary of BET analysis results for modified photocatalysts, including specific surface area, pore size distribution, and total pore volume.

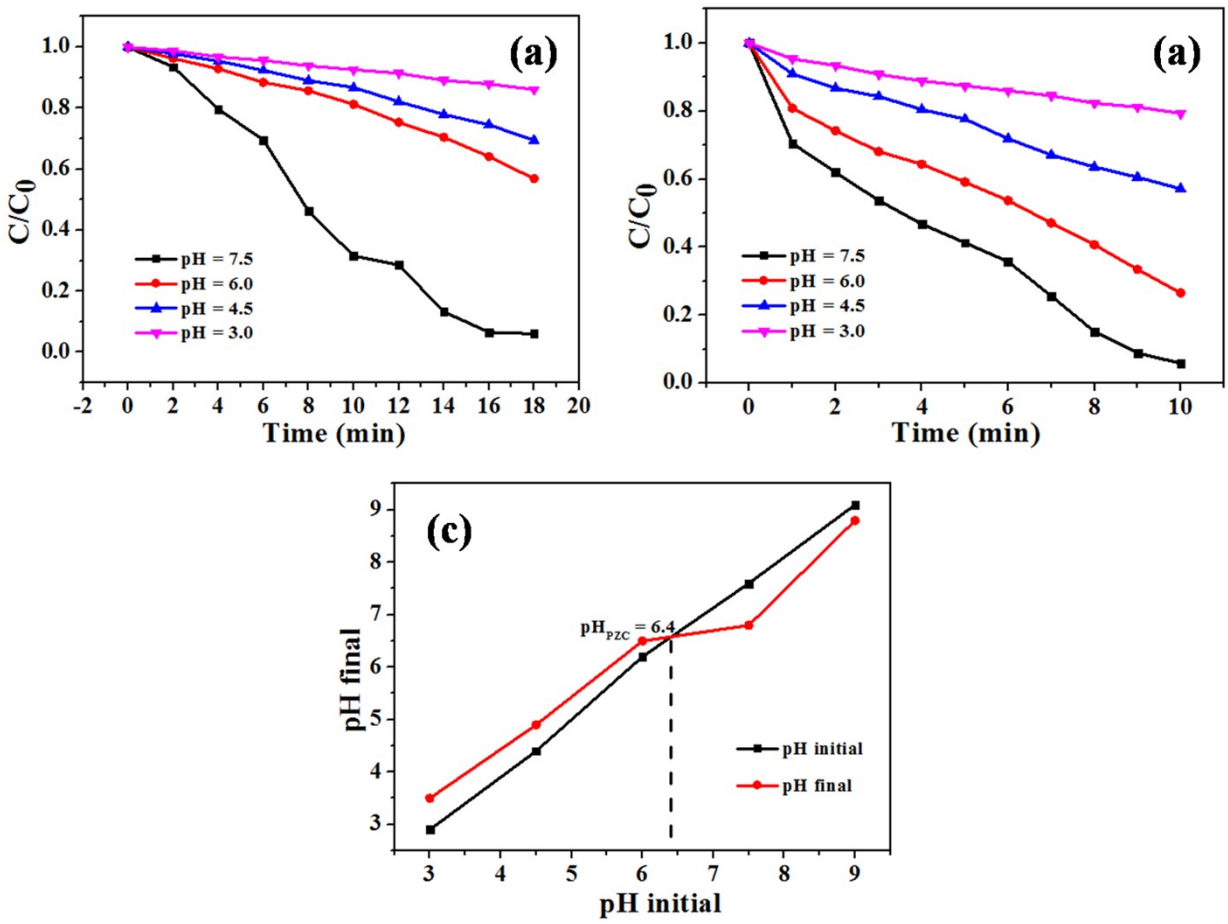

Fig. S10 Effect of pH on the photocatalytic degradation of (a) MB and (b) RhB using B-BiOBr/rGO as photocatalyst (c) The point of zero charge (pH_{PZC}) of B-BiOBr/rGO determined by the pH drift method.

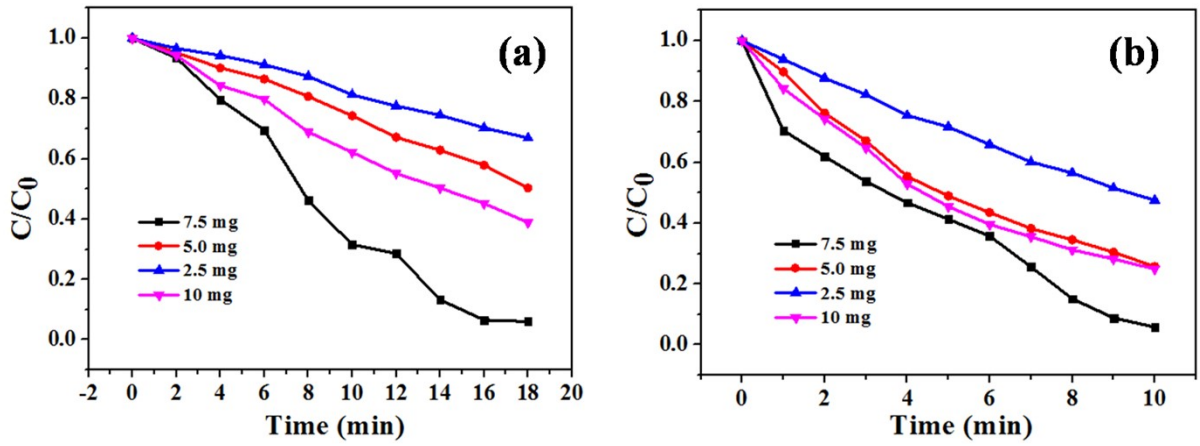

Fig. S11 Impact of catalyst loading on the photocatalytic degradation of (a) MB and (b) RhB using B-BiOBr/rGO photocatalyst.

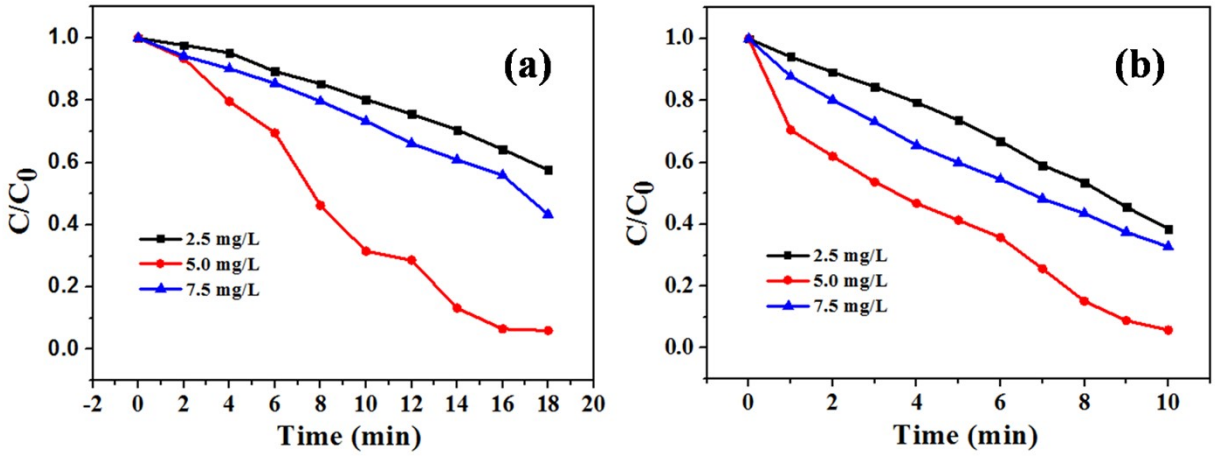

Fig. S12 Effect of initial dye concentration on the photocatalytic degradation of (a) MB and (b) RhB using B-BiOBr/rGO as the photocatalyst.

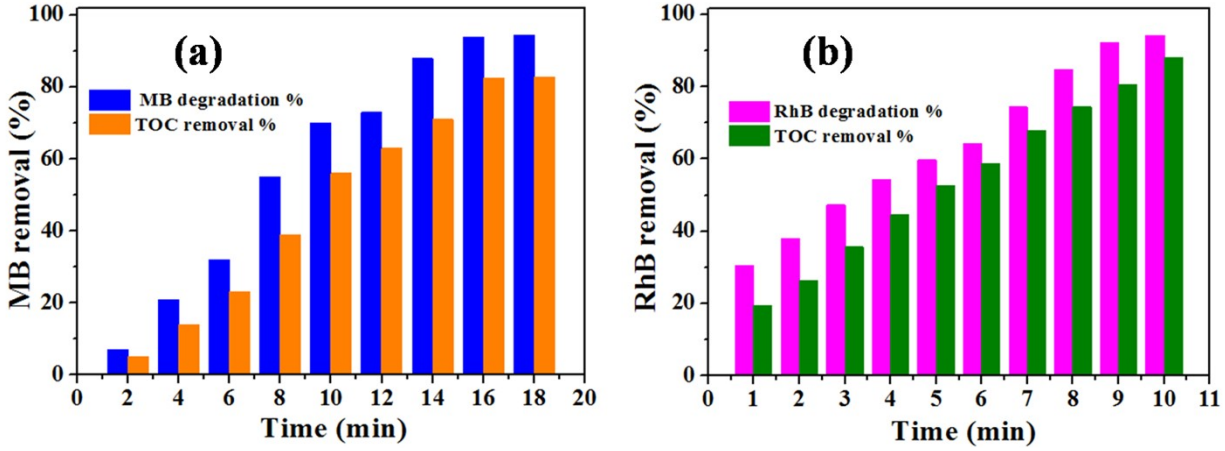

Fig. S13 Degradation efficiency and mineralization of (a) MB and (b) RhB by B-BiOBr/rGO under optimized conditions.

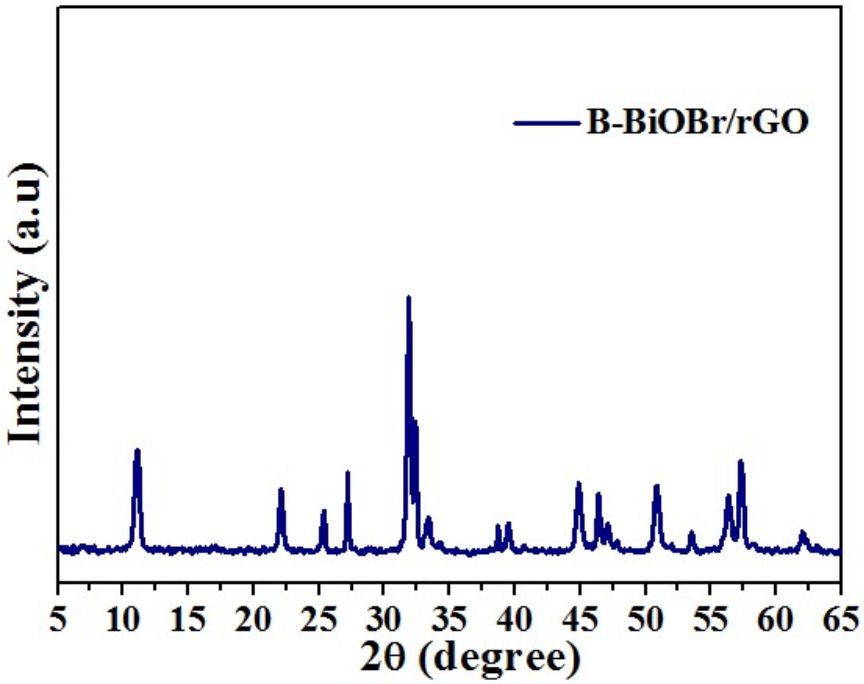

Fig. S14 XRD spectrum of B-BiOBr/rGO after photocatalytic activity studies.

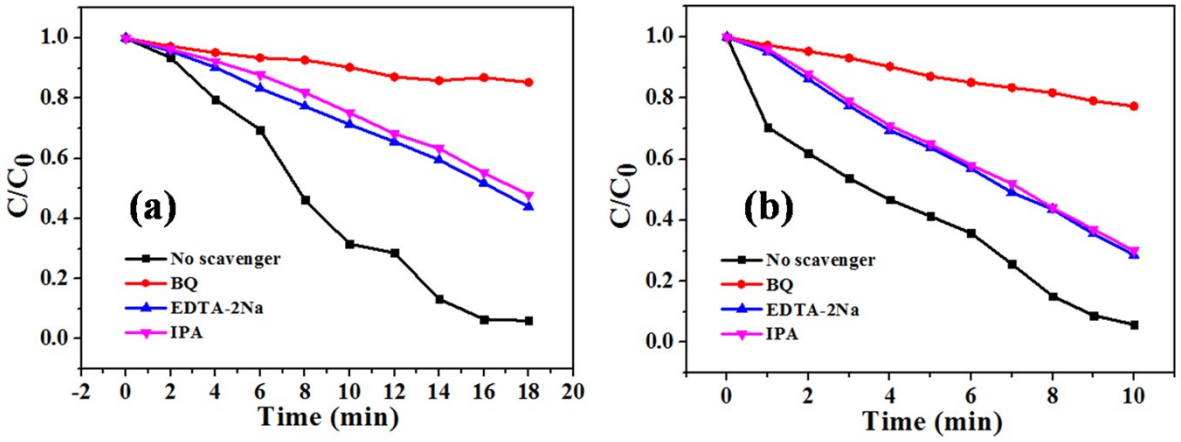

Fig. S15 Effect of scavengers on the photocatalytic degradation of (a) MB and (b) RhB using B-BiOBr/rGO as the catalyst.

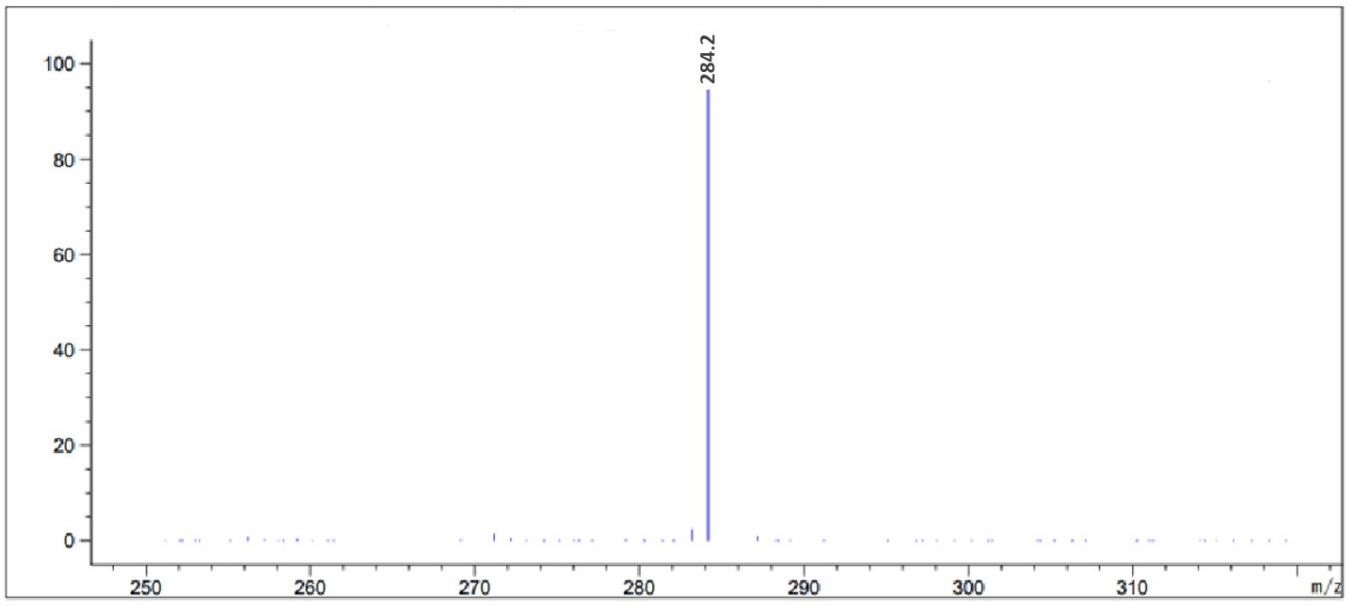

Fig. S16 LC–MS spectrum of methylene blue before light irradiation, showing the characteristic molecular ion peak of the parent dye.

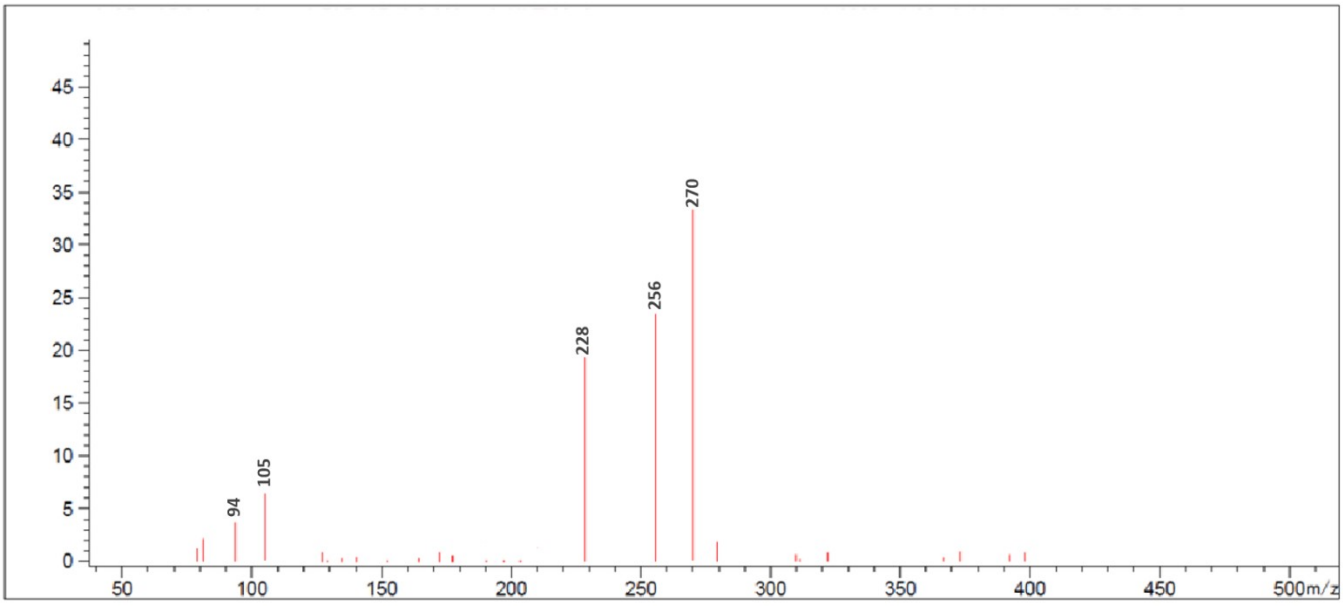

Fig. S17 LC–MS spectrum of methylene blue after photocatalysis, illustrating the degradation of the parent dye into characteristic fragment ions.

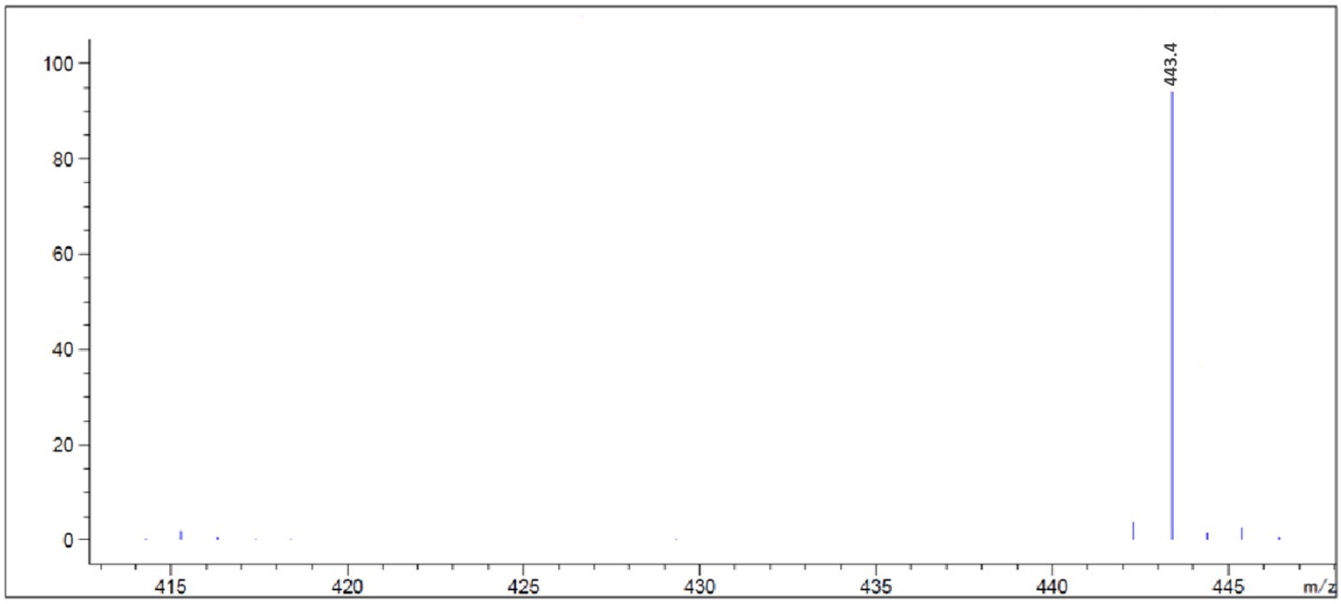

Fig. S18 LC–MS spectrum of rhodamine B before light irradiation, showing the characteristic molecular ion peak of the parent dye.

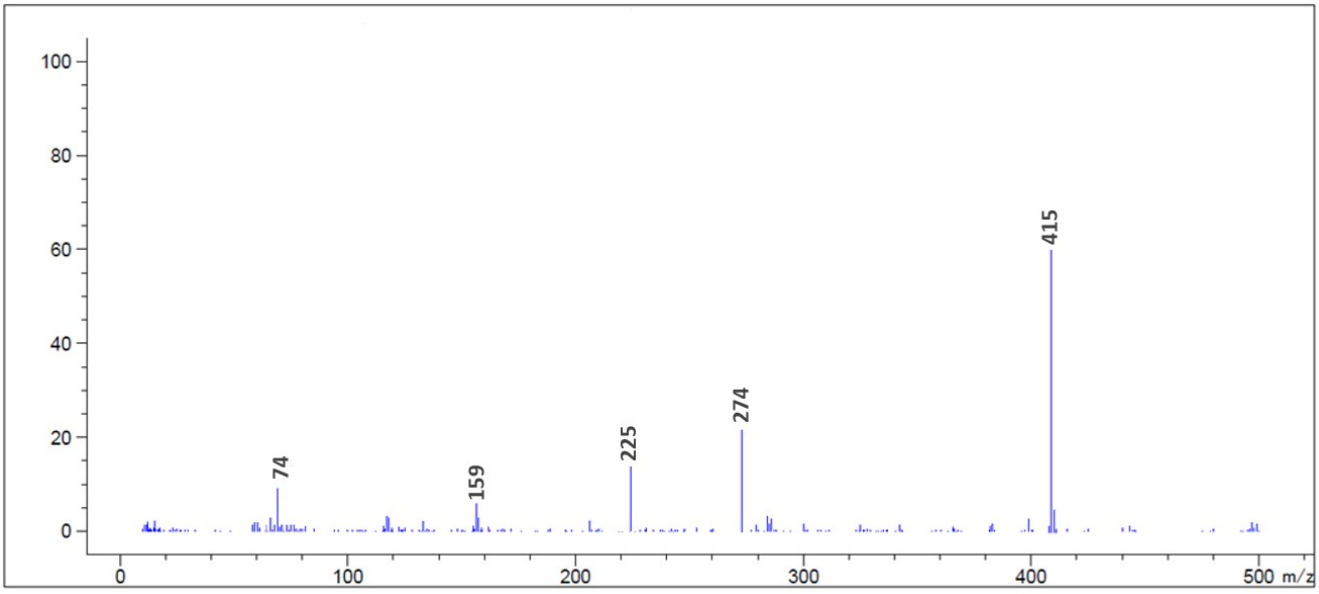

Fig. S19 LC–MS spectrum of rhodamine B after photocatalysis, illustrating the degradation of the parent dye into characteristic fragment ions.

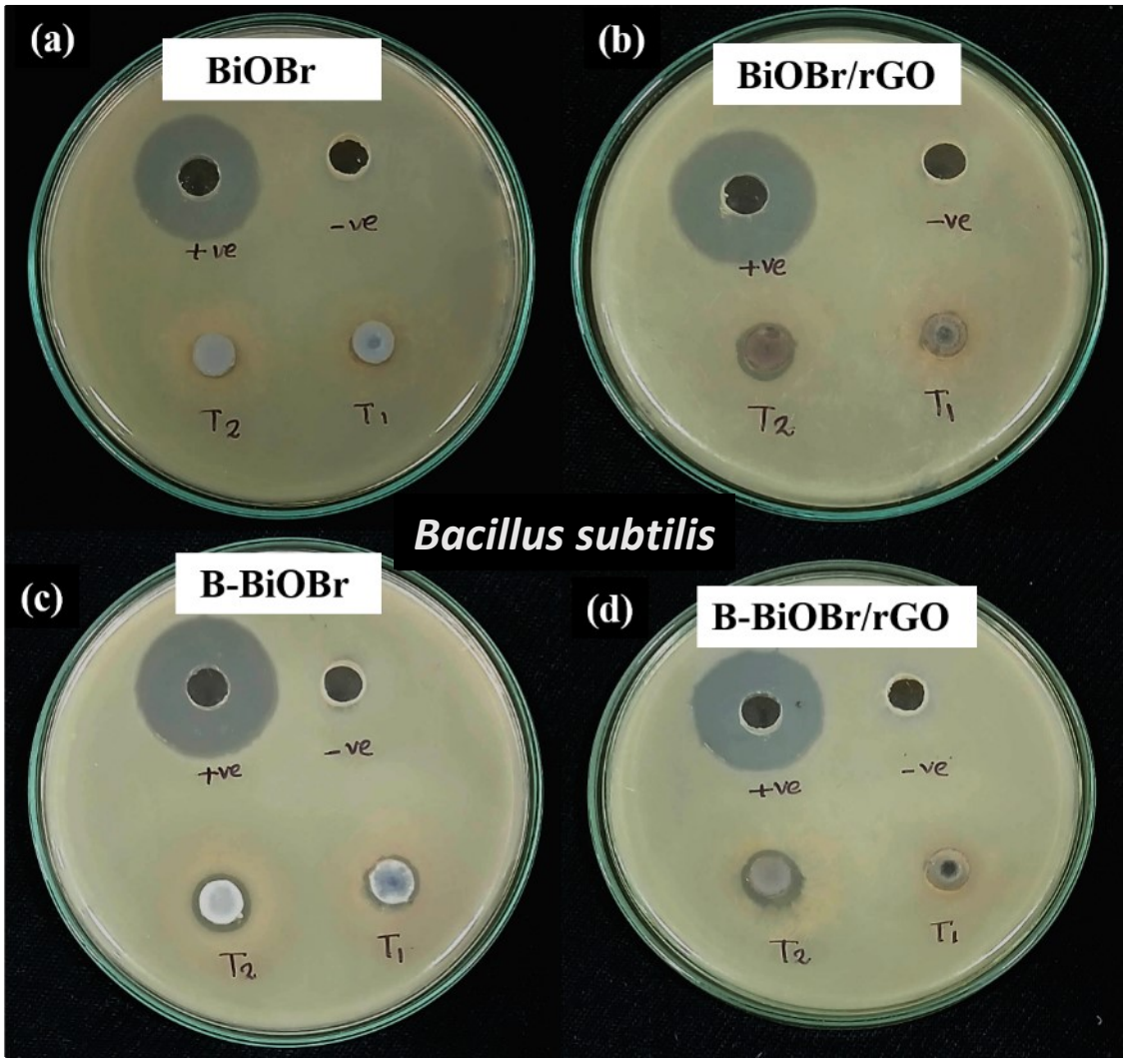

Fig. S20 Impact of varying concentrations of (a) BiOBr, (b) BiOBr/rGO, (c) B-BiOBr, and (d) B-BiOBr/rGO on the growth of Bacillus subtilis, a Gram-positive bacterium, at two different doses: 500 μg (T1) and 1000 μg (T2) per disc.

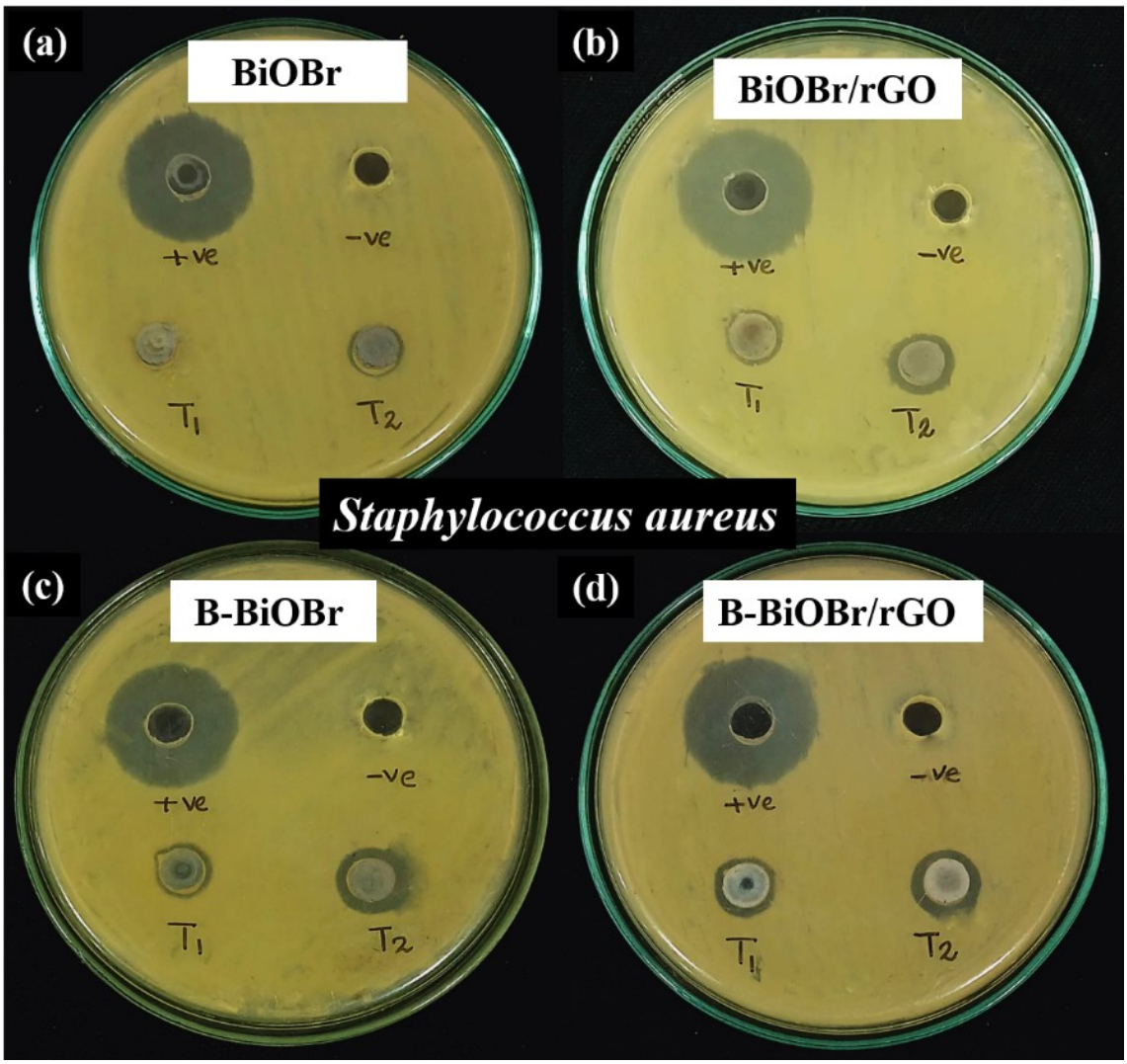

Fig. S21 Impact of varying concentrations of (a) BiOBr, (b) BiOBr/rGO, (c) B-BiOBr, and (d) B-BiOBr/rGO on the growth of Staphylococcus aureus, a Gram-positive bacterium, at two different doses: 500 µg (T1) and 1000 µg (T2) per disc.

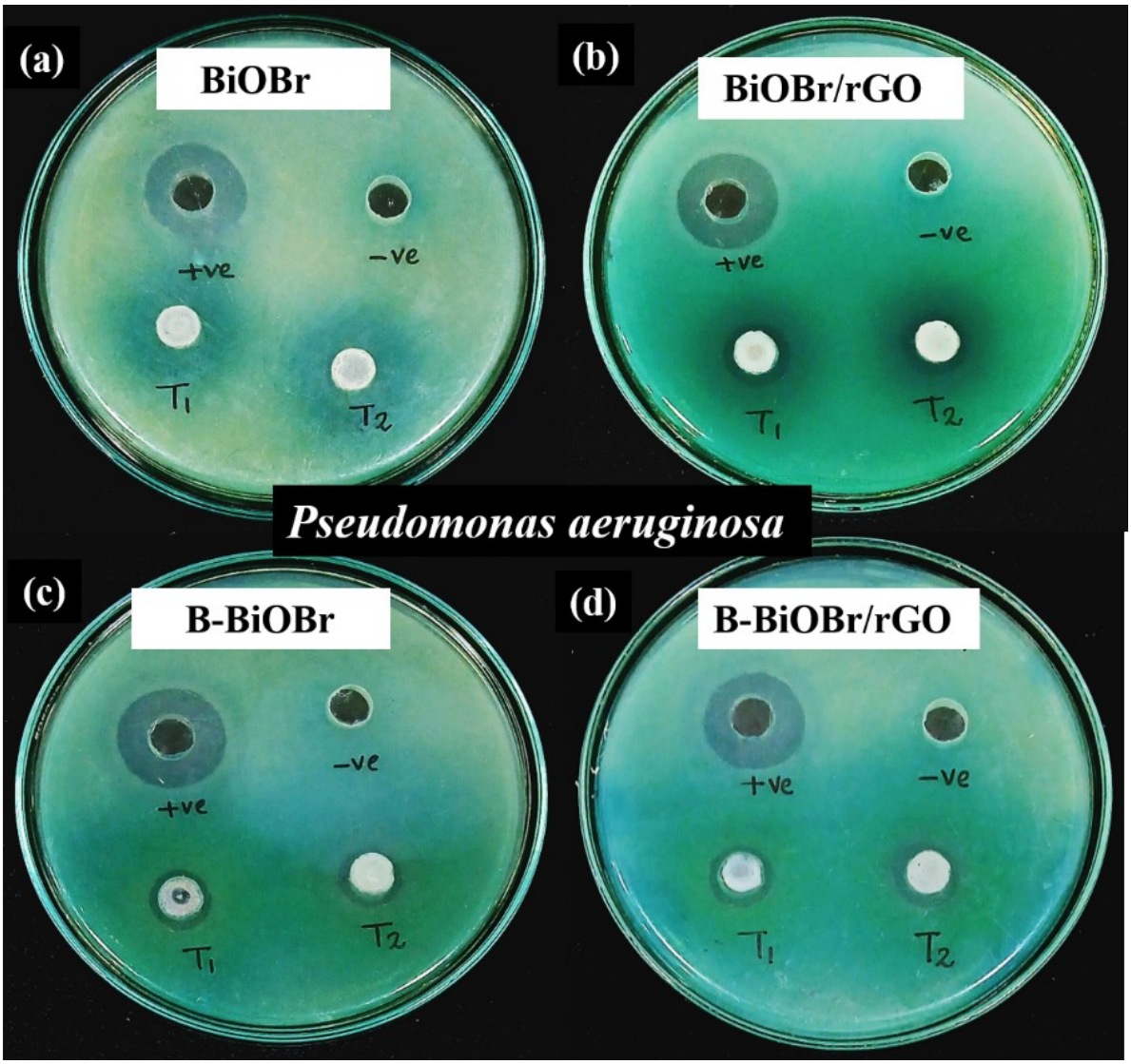

Fig. S22 Impact of varying concentrations of (a) BiOBr, (b) BiOBr/rGO, (c) B-BiOBr, and (d) B-BiOBr/rGO on the growth of Pseudomonas Aerugnosa, a Gram-negative bacterium, at two different doses: 500 μg (T1) and 1000 μg (T2) per disc.

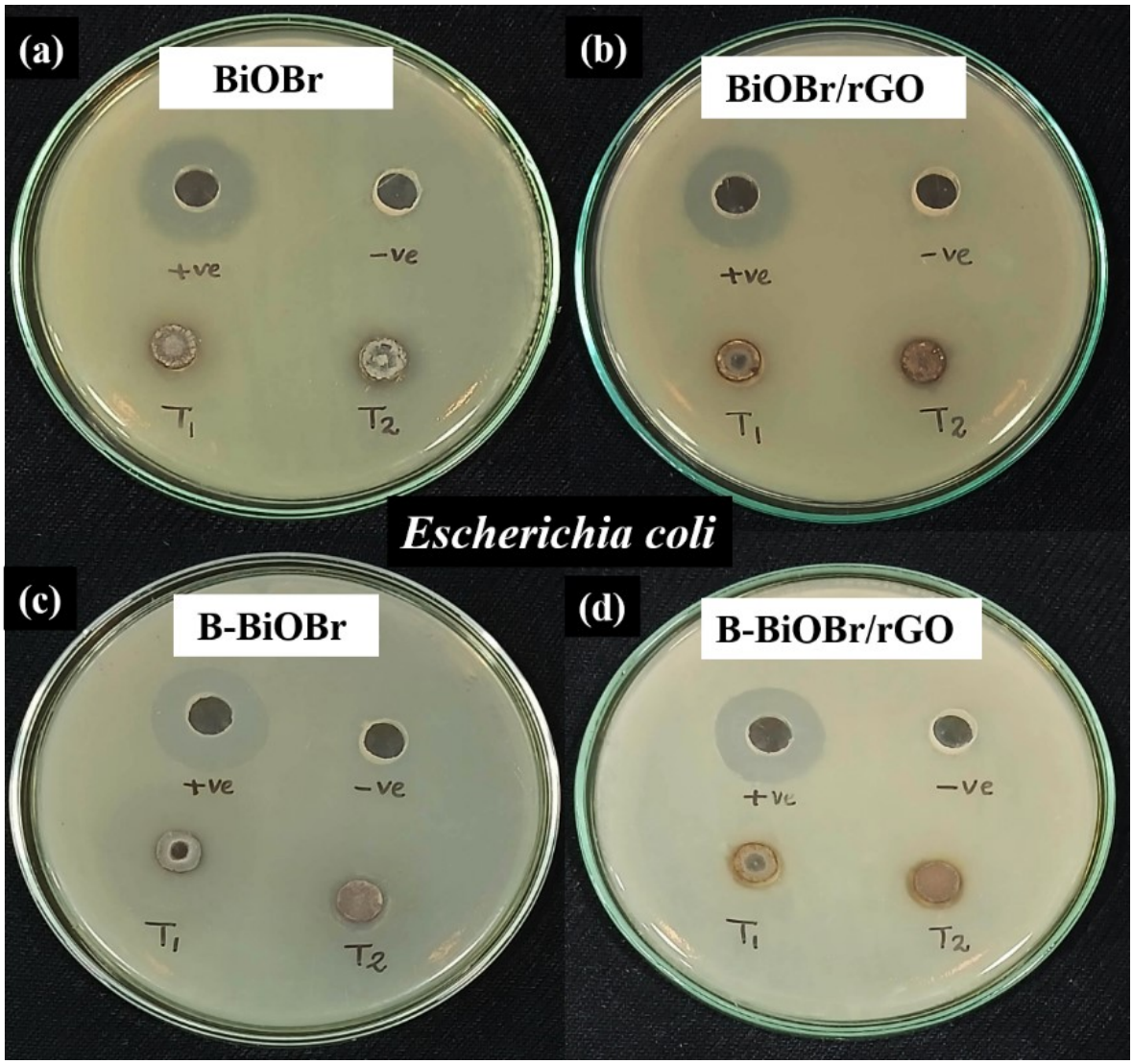

Fig. S23 Impact of varying concentrations of (a) BiOBr, (b) BiOBr/rGO, (c) B-BiOBr, and (d) B-BiOBr/rGO on the growth of Escherichia coli, a Gram-negative bacterium, at two different doses: 500 μg (T1) and 1000 μg (T2) per disc.

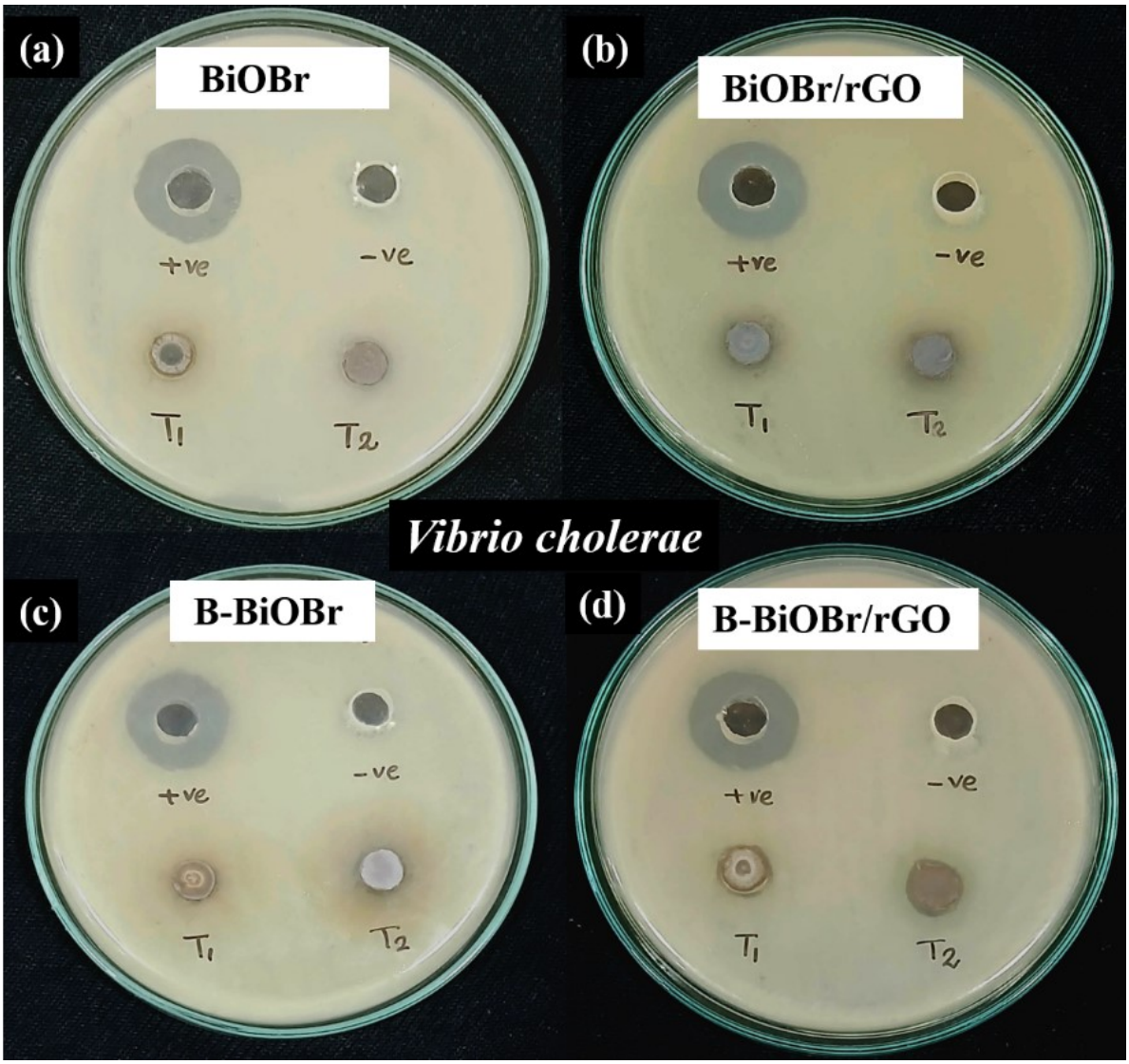

Fig. S24 Impact of varying concentrations of (a) BiOBr, (b) BiOBr/rGO, (c) B-BiOBr, and (d) B-BiOBr/rGO on the growth of Vibrio cholerae, a Gram-negative bacterium, at two different doses: 500 μg (T1) and 1000 μg (T2) per disc.

Name of Microorganism	Sample	Zone of Inhibition (ZOI in mm)			
		Positive control	Negative control	T_1(500µg)	T_2 (1000µg)
Pseudomonas aeruginosa	BiOBr	19	0	0	0
	BiOBr/rGO	19	0	11	13
	B-BiOBr	19	0	12	14
	B-BiOBr/rGO	19	0	12	15
Vibrio cholerae	BiOBr	20	0	0	0
	BiOBr/rGO	20	0	0	12
	B-BiOBr	20	0	0	13
	B-BiOBr/rGO	20	0	10	14
Escherichia coli	BiOBr	21	0	0	9
	BiOBr/rGO	21	0	0	10
	B-BiOBr	21	0	0	10
	B-BiOBr/rGO	21	0	9	11
Bacillus subtilis	BiOBr	25	0	0	0
	BiOBr/rGO	25	0	0	11
	B-BiOBr	25	0	0	11
	B-BiOBr/rGO	25	0	10	12
Staphylococcus aureus	BiOBr	25	0	0	9
	BiOBr/rGO	25	0	10	11
	B-BiOBr	25	0	10	11
	B-BiOBr/rGO	25	0	11	12

Table S3 Inhibition Zone Measurements for BiOBr, BiOBr/rGO, B-BiOBr, and B-BiOBr/rGO Against Different Bacterial Strains

Element	Mass	Conc.	Units
Bi	209	0.231	ppb

Table S4 ICP–MS analysis of B–BiOBr/rGO after antibacterial studies, showing Bi ion concentration to evaluate material stability.

Element	Mass	Conc.	Units
Bi	209	0.159	ppb

Table S5 ICP–MS analysis of B–BiOBr/rGO after photocatalytic degradation of methylene blue, demonstrating Bi ion release and structural stability of the composite.

Element	Mass	Conc.	Units
Bi	209	0.198	ppb

Table S6 ICP–MS analysis of B–BiOBr/rGO after photocatalytic degradation of rhodamine B, demonstrating Bi ion release and structural stability of the composite.